

Prediction of traffic oscillation instability with spectral analysis of the Aw–Rascle–Zhang model

Authors^a

^a*address*

Abstract

This article will focus on macroscopic second-order models as opposed to microscopic and mesoscopic frameworks.

Keywords:

1. Introduction

As personal vehicle ownership increases globally, traffic congestion continues to be a persistent problem. One goal of research in the physics of traffic is to gain a greater understanding of the phenomena, of which proper control would lead to mitigation of congestion. Traffic control strategies such as ramp metering and variable speed limits are in place today, but improved models of traffic dynamics could lay the foundations for more efficient coordination of control strategies.

What constitutes an “accurate” model often depends on the practitioners’ requirements. A model appropriate for a given application must describe key phenomena in the dynamics of the system under scrutiny so that they can be controlled efficiently. For traffic, a commonly used class of models relies on hydrodynamic theory, modeling vehicular flow in an aggregate manner. However, control schemes are only as reliable as the models on which they are based. Thus, given that each model can only reproduce some features of traffic flow, a challenge of traffic engineering is the selection of the model most appropriate for the application of interest. We first start with a short summary of history of models leading to the model of interest in this article.

1.1. First-order models

The 1950’s saw the development of the *Lighthill–Whitham–Richards* (LWR) model [1, 2], which became the seminal model for aggregate traffic flow. The dynamics of this first-order scalar hyperbolic conservation law is governed by

$$\rho_t + (Q(\rho))_x = 0, \tag{1}$$

where ρ is the lineic vehicular density (veh/m), and $Q(\rho)$ is the empirically measured traffic flux (veh/s), also referred to as the fundamental diagram. Numerous phenomenological models exist for $Q(\rho)$, such as the Greenshields model [3], the Greenberg model [4], the triangular model, [5, 6], power law models, [7, 8] and many others. The simplicity of the LWR model enabled the formulation of numerical discretization schemes such as the Godunov scheme [9, 10], later renamed the cell transmission model [6, 11] in the transportation community.

First-order models have inherent shortcomings, most of which are discussed at length in [12], such as failure to capture accurately shock structure, light traffic dynamics, and stop-and-go behavior, otherwise known as traffic oscillations. The last phenomenon in particular has attracted increasing attention in transportation research. For example jamitons, traffic jams that appear without the presence of a bottleneck, have been reproduced in contained experiments [13, 14] and explained theoretically as the result of both particular configurations of the traffic system [15] and fuzzy fundamental diagrams [16].

1.2. First-generation second-order models

In an effort to refine traffic modeling, Payne and Whitham followed the same approach as in fluid dynamics developed a higher-order model to capture momentum-related features [17, 18]. The *Payne–Whitham* (PW) model consists of a mass conservation equation as in the LWR model,

$$\rho_t + (\rho v)_x = 0, \quad (2)$$

where ρ and v are the density and velocity, respectively. This is seconded by a momentum equation,

$$v_t + vv_x + \frac{p'(\rho)}{\rho} \rho_x = \frac{V(\rho) - v}{\tau} + \nu v_{xx}, \quad (3)$$

where the pressure function, $p(\rho)$, is strictly increasing and the equilibrium speed, $V(\rho)$, is nonincreasing. Both are empirically measured and $V(\rho)$ satisfies $Q(\rho) = \rho V(\rho)$. The parameters τ and ν are nonnegative, representing the relaxation time and coefficient of viscosity, respectively. This approach, however, has issues in both the derivation of its equations, and its predictions [12]. The PW model relies on the assumption that spacing and speed vary slowly, yielding negligible second and third derivatives for these quantities. This is contradictory with the observations of Newell [19] given that the car-following model predicts sharp changes in these quantities. Also, the PW model violates the anisotropy of traffic flow and can predict negative speeds [20].

1.3. Second-generation second-order models

Despite the criticism expressed in [12] regarding higher-order models inspired by fluid dynamics, Zhang proposed improved models to resolve issues plaguing earlier second-order models. In [21], he proposed a modification of the momentum equation of the PW model to handle the issue of backward-propagating traffic. Soon after, Aw and Rascle [22] presented a model with the following momentum equation:

$$\frac{\partial(v + p(\rho))}{\partial t} + v \frac{\partial(v + p(\rho))}{\partial x} = \frac{V(\rho) - v}{\tau}. \quad (4)$$

Including the pressure term, $p(\rho)$, in a convective derivative guarantees that no information travels faster than the speed of the cars. Aw and Rascle demonstrated in [22] that “with a suitable choice of function p ,” the above class of models avoids inconsistencies of earlier second-order models. Zhang proposed in [20] the same model with $p(\rho) = -V(\rho)$. With this choice of $p(\rho)$, the model is referred to as the *Aw–Rascle–Zhang* (ARZ) model, which is the model used in the present article.

This model has since been thoroughly studied. The work in [22] concluded that a relaxation term accounting for traffic equilibrium was needed so the speed of cars would be determined by the fundamental diagram and not the initial data. Rascle later proved in [23] that the relaxed model converges towards the LWR model as $\tau \rightarrow 0$. The first ARZ model requires a fundamental diagram extended to negative and maximum speeds, and zero and maximum densities so as to guarantee solutions to the Riemann problem and stability with low densities [24]. In [25], discretization enabled extension of the AR model to a network setup with junctions and traffic lights. With an extended fundamental diagram, any Riemann problem for the ARZ model can be solved, allowing for a Godunov discretization scheme and numerical comparison in which the ARZ model fits real data better than the LWR model [26].

More recently a generalized model proposed in [27] corrects the fact that, in the ARZ model, several maximum densities co-exist, seemingly contradictory to the intuition that this quantity is uniquely determined by the characteristics of the freeway. Although more realistic, such a model does not allow proper linearization about an equilibrium which is a procedure core to this article so as to make second order models more practically tractable.

1.4. Models appropriate for control

It is mentioned in [27] that for congested regimes, the LWR model tends to offer a slightly better fit than the ARZ model with respect to empirical measurements but is outperformed for low densities. Ideally we would use a model suitable for all regimes so as to establish generic control strategies for traffic. Because such a model does not exist, we choose instead to develop the ARZ model linearized around arbitrary nominal

conditions. Specific classes of second-order models, including the ARZ model in particular, realistically account for traffic oscillations in dense traffic [28]. Laplace transform and spectral analysis are powerful tools for control problems, providing a simple yet holistic representation of a system. In this regard, it is important to have a model that predicts oscillatory phenomena. Behavioral models such as in [19], and more recently [29], depict in a detailed fashion the effects of car-following and lane-changing on freeway dynamics, effects often cited as the cause of oscillations [30, 31, 32]. However, second-order macroscopic models are most suited for our method.

Fourier and Laplace transforms are not the only spectral operators that can be used to study traffic. Approaches such as [33] attempt to model spectral features of traffic using wavelets so as to account for turbulent phenomena on various scales of time. The method we follow here is different as it is mostly driven by macroscopic physics of traffic rather than data driven analysis.

1.5. Similarities with Saint-Venant equations

Our control analysis of the ARZ equations is strongly inspired by the pioneering analysis of Litrico and Fromion for the Saint-Venant equations, see in particular the monograph [34]. The Saint-Venant equations are as follows:

$$T \frac{\partial y}{\partial t} + \frac{\partial q}{\partial x} = 0, \quad (5)$$

$$\frac{\partial v}{\partial t} + v \frac{\partial v}{\partial x} + g \frac{\partial y}{\partial x} = g (S_b - S_f), \quad (6)$$

where v is the fluid velocity in a canal, q the flux, T the top width, y the water height, S_f the friction slope, and S_b the bed slope. Note the structural similarity to the ARZ equations. In the equilibrium regime, the term $S_b - S_f(x, t)$ is zero under uniform flow, making it analogous to the relaxation term $\frac{V(\rho) - v}{\tau}$, defined to be zero at the equilibrium. Linearizing this system around an equilibrium point enables the use of spectral methods to design efficient control strategies for canals [35] thus enabling hydrodynamicists to use control theory effectively. Approximations for the low frequency domain decompose the transfer matrix into a combination of delay and integration components, allowing for design of efficient PI controllers while enabling a simpler theoretical analysis of hydraulic systems [34, 35].

1.6. Approach and contributions

The present article adapts the corresponding spectral framework of [34] to the case of the ARZ equations so as to achieve a two-fold objective:

- We aim to develop strategies that enforce ease of use of the ARZ model for stability analysis and control. Analytical solutions to these non-linear equations are difficult to derive but linearization facilitates design of efficient control schemes with multiple inputs and outputs. We pay particular attention to the formulation of boundary conditions, to guarantee the well-posedness of the problem.
- We assess fit quality of the model by comparing its output with actual data collected in the field (using the NGSIM dataset).

The contributions of this article are as follows:

- *Modeling*: We derive the characteristic form by linearization and diagonalization of the ARZ model. This form highlights important features of the model, leading to the definition of a counterpart to the Froude number in hydrodynamics [34], separating free-flow and congested regimes.
- *Spectral analysis*: From the characteristic form we derive the spectral form. Time domain responses derived from the spectral transfer matrices show that the linearized system is unstable in the free-flow regime and accounts for nonlinear wave propagation, giving rise to jamitons. These waves occur for an entire set of values of velocity, density, and flux and lead the linearized system away from its equilibrium point in the free-flow regime.

- *Numerical validation:* A numerical experiment using NGSIM data is conducted to verify that linearization does not destroy realistic properties of the ARZ model. Previous studies also using NGSIM data to assess predictions of second-order models focused on averaged errors and only displayed predictions at a couple of points along the freeway [26, 27]. Here, we show an entire map of the states and conduct model assessment in a holistic manner, providing a complete analysis of the strengths and weaknesses of the model to be used for control. Our estimation procedure, unlike [27], does not rely on any assumption about the typical vehicle length or the safety distance factor. Additionally, no discretization scheme is needed and no grid size condition needs to be fulfilled. This procedure proves that the linearized model successfully accounts for traffic oscillations and also provides simple and consistent methods to calibrate the relaxation time, τ .

1.7. Organization of the article

The rest of this article is organized as follows. In Section 2 we present the characteristic form of the ARZ model in several state variables, leading to the derivation of the spectral form of the flux and velocity system in section 3. We focus on these states in particular as they are the most easily observed and controlled in traffic. Properties of the spectral form in the two flow regimes are also analyzed. Section 4 focuses on numerical analysis. We present estimation procedures for (v, q, ρ) and the model parameters, comparing empirical estimates with numerical predictions of the linearized model. We use *Fast Fourier Transform* (FFT) to turn the spectral model into a prediction tool.

2. The ARZ model

We consider the ARZ model with relaxation term. The model is shown here:

$$\rho_t + (\rho v)_x = 0, \quad (7)$$

$$(v - V(\rho))_t + v(v - V(\rho))_x = \frac{V(\rho) - v}{\tau}, \quad (8)$$

where ρ is the density, v is the velocity, τ is the relaxation time, and $V(\rho) = Q(\rho)/\rho$ is the equilibrium velocity profile, where $Q(\rho)$ is the density-flow relation given by the fundamental diagram. Without the relaxation term cars never reach the maximum allowable speed [23]. Note that at the equilibrium velocity this term is zero.

In vector form the ARZ model is

$$\begin{pmatrix} \rho \\ v \end{pmatrix}_t + \begin{pmatrix} v & \rho \\ 0 & v + \rho V'(\rho) \end{pmatrix} \begin{pmatrix} \rho \\ v \end{pmatrix}_x = \begin{pmatrix} 0 \\ \frac{V(\rho) - v}{\tau} \end{pmatrix}. \quad (9)$$

With the appropriate variable change, we can rewrite the model in the density-flow and velocity-flow forms, the latter of which is most useful to us for practical control purposes. Using the flow relation $q = \rho v$ and (9), the density-flow form is

$$\begin{pmatrix} \rho \\ q \end{pmatrix}_t + \begin{pmatrix} 0 & 1 \\ -\frac{q}{\rho} \left(\frac{q}{\rho} + \rho V'(\rho) \right) & 2\frac{q}{\rho} + \rho V'(\rho) \end{pmatrix} \begin{pmatrix} \rho \\ q \end{pmatrix}_x = \begin{pmatrix} 0 & 0 \\ \frac{V(\rho)}{\tau} & -\frac{1}{\tau} \end{pmatrix} \begin{pmatrix} \rho \\ q \end{pmatrix}. \quad (10)$$

In the same manner we arrive at the velocity-flow form,

$$\begin{pmatrix} v \\ q \end{pmatrix}_t + \begin{pmatrix} v + \frac{q}{v} V' \left(\frac{q}{v} \right) & 0 \\ \frac{q}{v} \left(v + \frac{q}{v} V' \left(\frac{q}{v} \right) \right) & v \end{pmatrix} \begin{pmatrix} v \\ q \end{pmatrix}_x = \frac{1}{\tau} \begin{pmatrix} V \left(\frac{q}{v} \right) - v \\ \frac{q}{v} V \left(\frac{q}{v} \right) - q \end{pmatrix}. \quad (11)$$

Note that the (ρ, q) or (v, q) forms are less common in transportation engineering but present interesting similarities with hydrodynamics. Moreover, they are promising for sensing problems. Loop detectors typically sense (ρ, q) whereas GPS measurement generally yield estimates for (v, q) .

2.1. Linearization

We are interested in small deviations, $(\tilde{\rho}(x, t), \tilde{v}(x, t))$, from a given nominal profile. Consider the nominal solution $(\rho^*(x), v^*(x))(V(\rho^*) = v^*)$ satisfying $v_t = \rho_t = 0$. Then (9) becomes

$$v^* \frac{d\rho^*}{dx} + \frac{dv^*}{dx} \rho^* = 0, \quad (12)$$

$$(v^* + \rho^* V'(\rho^*)) \frac{dv^*}{dx} = \frac{V(\rho^*) - v^*}{\tau} = 0. \quad (13)$$

Then we must have $v_x^* = \rho_x^* = 0$, so the solution is uniform along the road.

Linearizing the ARZ model (9) around the nominal solution described above, we obtain

$$\begin{pmatrix} \tilde{\rho} \\ \tilde{v} \end{pmatrix}_t + \begin{pmatrix} v^* & \rho^* \\ 0 & v^* + \rho^* V'(\rho^*) \end{pmatrix} \begin{pmatrix} \tilde{\rho} \\ \tilde{v} \end{pmatrix}_x = \begin{pmatrix} 0 & 0 \\ \frac{V'(\rho^*)}{\tau} & -\frac{1}{\tau} \end{pmatrix} \begin{pmatrix} \tilde{\rho} \\ \tilde{v} \end{pmatrix} \quad (14)$$

Similarly for the density-flow system (10), we linearize around the equilibrium $(\rho^*, q^*)(\rho^* V(\rho^*) = q^*)$ with deviations $(\tilde{\rho}(x, t), \tilde{q}(x, t))$. The linearized system is as follows

$$\begin{pmatrix} \tilde{\rho} \\ \tilde{q} \end{pmatrix}_t + \begin{pmatrix} 0 & 1 \\ \alpha^* \beta^* & \alpha^* - \beta^* \end{pmatrix} \begin{pmatrix} \tilde{\rho} \\ \tilde{q} \end{pmatrix}_x = \begin{pmatrix} 0 & 0 \\ \delta & \sigma \end{pmatrix} \begin{pmatrix} \tilde{\rho} \\ \tilde{q} \end{pmatrix}, \quad (15)$$

where $\alpha^* = \frac{q^*}{\rho^*}$, $\beta^* = -\frac{q^*}{\rho^*} - \rho^* V'(\rho^*)$, $\delta = \frac{V(\rho^*) + \rho^* V'(\rho^*)}{\tau}$, and $\sigma = -\frac{1}{\tau}$.

Finally, for the velocity-flow system,

$$\begin{pmatrix} \tilde{v} \\ \tilde{q} \end{pmatrix}_t + \underbrace{\begin{pmatrix} v^* + \frac{q^*}{v^*} V'(\frac{q^*}{v^*}) & 0 \\ \frac{q^*}{v^*} (v^* + \frac{q^*}{v^*} V'(\frac{q^*}{v^*})) & v^* \end{pmatrix}}_A \begin{pmatrix} \tilde{v} \\ \tilde{q} \end{pmatrix}_x = \underbrace{\begin{pmatrix} -\frac{(v^*)^2 + q^* V'(\frac{q^*}{v^*})}{(v^*)^2 \tau} & \frac{V'(\frac{q^*}{v^*})}{v^* \tau} \\ \frac{q^* ((v^*)^2 + q^* V'(\frac{q^*}{v^*}))}{(v^*)^3 \tau} & \frac{q^* V'(\frac{q^*}{v^*})}{(v^*)^2 \tau} \end{pmatrix}}_B \begin{pmatrix} \tilde{v} \\ \tilde{q} \end{pmatrix}. \quad (16)$$

2.2. Characteristic form

We rewrite the model in the characteristic form by diagonalizing the linearized equations. We begin with the density-flow system. Standard algebraic manipulations of the equations in (14) lead to:

$$\begin{pmatrix} \zeta_1 \\ \zeta_2 \end{pmatrix}_t + \begin{pmatrix} \lambda_1 & 0 \\ 0 & \lambda_2 \end{pmatrix} \begin{pmatrix} \zeta_1 \\ \zeta_2 \end{pmatrix}_x = \begin{pmatrix} -\frac{1}{\tau} & 0 \\ -\frac{1}{\tau} & 0 \end{pmatrix} \begin{pmatrix} \zeta_1 \\ \zeta_2 \end{pmatrix}, \quad (17)$$

where $\zeta_1 = \tilde{v} - V'(\rho^*) \tilde{\rho}$ and $\zeta_2 = \tilde{v}$ are the Riemann invariants of the (ρ, v) system, and $\lambda_1 = v^*$ and $\lambda_2 = v^* + \rho^* V'(\rho^*)$ are the eigenvalues. Note that $V'(\rho^*) < 0$ so $\lambda_2 \leq \lambda_1 = v^*$. Therefore this is consistent with the physical dynamics of the system as no waves travel faster than the equilibrium vehicle speed.

We proceed in the same manner as above to diagonalize the (ρ, q) system (15). The diagonal form is

$$\begin{pmatrix} \chi_1 \\ \chi_2 \end{pmatrix}_t + \begin{pmatrix} \lambda_1 & 0 \\ 0 & \lambda_2 \end{pmatrix} \begin{pmatrix} \chi_1 \\ \chi_2 \end{pmatrix}_x = \begin{pmatrix} -\frac{1}{\tau} & 0 \\ -\frac{1}{\tau} & 0 \end{pmatrix} \begin{pmatrix} \chi_1 \\ \chi_2 \end{pmatrix}, \quad (18)$$

where $\chi_1 = -\lambda_2 \tilde{\rho} + \tilde{q}$ and $\chi_2 = -\lambda_1 \tilde{\rho} + \tilde{q}$ are the characteristic variables in the (ρ, q) system and the eigenvalues λ_1 and λ_2 are the same as in the density-velocity system due to the relation $q^* = \rho^* v^*$.

Diagonalization of the velocity-flow system is more involved. Letting $\xi(x, t) = (\tilde{v}, \tilde{q})^T$, we can rewrite (16) as

$$\eta_t + A \eta_x = B \eta. \quad (19)$$

The eigenvalues of A are $\lambda_1 = v^*$ and $\lambda_2 = v^* + \frac{q^*}{v^*} V' \left(\frac{q^*}{v^*} \right)$, consistent with the previous systems. Then A can be diagonalized as follows

$$A = XDX^{-1}, \quad (20)$$

$$X = \begin{pmatrix} 0 & \lambda_2 - \lambda_1 \\ 1 & \rho^* \lambda_2 \end{pmatrix}, \quad (21)$$

$$D = \begin{pmatrix} \lambda_1 & 0 \\ 0 & \lambda_2 \end{pmatrix}, \quad (22)$$

$$X^{-1} = \begin{pmatrix} \frac{\rho^* \lambda_2}{\lambda_1 - \lambda_2} & 1 \\ -\frac{1}{\lambda_1 - \lambda_2} & 0 \end{pmatrix}. \quad (23)$$

Define $\gamma(x, t) := X\eta(x, t)$. Hence (19) can be rewritten as

$$\gamma_t + \begin{pmatrix} \lambda_1 & 0 \\ 0 & \lambda_2 \end{pmatrix} \gamma_x = \begin{pmatrix} -\frac{1}{q^* \tau} & 0 \\ -\frac{1}{q^* \tau} & 0 \end{pmatrix} \gamma \quad (24)$$

where

$$\gamma = \begin{pmatrix} \frac{\rho^* \lambda_2}{\lambda_1 - \lambda_2} \tilde{v} + \tilde{q} \\ -\frac{1}{\lambda_1 - \lambda_2} \tilde{v} \end{pmatrix}. \quad (25)$$

Let $\xi = (\xi_1, \xi_2)^T = (\chi_1, -q^* \chi_2)^T$. Then we have

$$\begin{pmatrix} \xi_1 \\ \xi_2 \end{pmatrix}_t + \begin{pmatrix} \lambda_1 & 0 \\ 0 & \lambda_2 \end{pmatrix} \begin{pmatrix} \xi_1 \\ \xi_2 \end{pmatrix}_x = \begin{pmatrix} -\frac{1}{\tau} & 0 \\ -\frac{1}{\tau} & 0 \end{pmatrix} \begin{pmatrix} \xi_1 \\ \xi_2 \end{pmatrix}, \quad (26)$$

and

$$\begin{pmatrix} \xi_1 \\ \xi_2 \end{pmatrix} = \begin{pmatrix} \frac{\rho^* \lambda_2}{\lambda_1 - \lambda_2} \tilde{v} + \tilde{q} \\ \frac{q^*}{\lambda_1 - \lambda_2} \tilde{v} \end{pmatrix} = \begin{pmatrix} \frac{\rho^* \lambda_2}{\lambda_1 - \lambda_2} & 1 \\ \frac{\rho^* \lambda_1}{\lambda_1 - \lambda_2} & 0 \end{pmatrix} \begin{pmatrix} \tilde{v} \\ \tilde{q} \end{pmatrix} \quad (27)$$

2.3. The Traffic Froude Number

In fluid mechanics, the Froude number is a dimensionless number which delineates the boundary between flow regimes [36, 34]. Using the eigenvalues of the system in the characteristic form, we are able to define a useful counterpart to this number. Since $V(\rho)$ is nonincreasing function, we have $V'(\rho^*) \leq 0$. Thus there are two flow regimes, one where $\lambda_1 \lambda_2 < 0$ and one characteristic curve travels downstream, and one where $\lambda_1 \lambda_2 > 0$ and both characteristic curves travel upstream.

We define the *Traffic Froude Number* (TFN) as

$$F = \frac{\rho^* V'(\rho^*)}{v^*}. \quad (28)$$

Then we have

$$\begin{cases} F > 1 & \Rightarrow |\rho^* V'(\rho^*)| > v^* & \Rightarrow \lambda_2 < 0 \\ F < 1 & \Rightarrow |\rho^* V'(\rho^*)| < v^* & \Rightarrow \lambda_2 > 0 \end{cases}.$$

Note also that $\lambda_2 = v^* + \rho^* V'(\rho^*) = \frac{Q(\rho^*)}{\rho^*} + \frac{\rho^* Q'(\rho^*) - Q(\rho^*)}{\rho^*} = Q'(\rho^*)$. Hence the system is in free-flow when $F < 1$ and congestion when $F > 1$. In hydrodynamics these regimes are referred to as the supercritical and subcritical regimes, respectively [34]. For traffic, the interpretation of the different regimes is somewhat different. Free flow regime corresponds to these situations where drivers are not slowed down by heavy traffic and go as fast as the authorized speed. The congested regime arises when traffic is denser and, because too many cars are present on the same freeway section, drivers slow down and eventually form traffic jam.

3. Spectral analysis of the linearized ARZ model

We now consider the (v, q) system for the frequency domain analysis for practical control purposes.

3.1. State-transition matrix

Taking the Laplace transform of the diagonalized form (26) we obtain

$$\frac{\partial \hat{\zeta}(x, s)}{\partial x} = \mathcal{A}(s) \hat{\zeta}(x, s) + \mathcal{B} \zeta(x, t = 0^-), \quad (29)$$

where $\mathcal{A}(s) = A^{-1}(B - sI)$ and $\mathcal{B} = -A^{-1}$. The general solution to this ordinary differential equation is

$$\hat{\zeta}(x, s) = \Phi(x, s) \hat{\zeta}(0, s) + \Phi(x, s) \int_0^x \Phi(\nu, s)^{-1} \mathcal{B} \zeta(\nu, 0^-) d\nu, \quad (30)$$

where $\Phi(x, s) = e^{\mathcal{A}(s)x}$ is the state-transition matrix. Assuming zero initial conditions we have

$$\hat{\zeta}(x, s) = \Phi(x, s) \hat{\zeta}(0, s). \quad (31)$$

To compute the exponential we diagonalize the matrix as

$$\mathcal{A}(s) = \mathcal{X}(s) \mathcal{D}(s) \mathcal{X}^{-1}(s) \quad (32)$$

where

$$\mathcal{X}(s) = \begin{pmatrix} 0 & \frac{\lambda_2 - (\lambda_1 - \lambda_2)\tau s}{\lambda_1} \\ 1 & 1 \end{pmatrix}, \quad (33)$$

$$\mathcal{D}(s) = \begin{pmatrix} -\frac{s}{\lambda_2} & 0 \\ 0 & -\frac{1+\tau s}{\tau \lambda_1} \end{pmatrix}. \quad (34)$$

Hence

$$\Phi(x, s) = \mathcal{X}^{-1}(s) e^{\mathcal{D}(s)x} \mathcal{X}(s) = \begin{pmatrix} \phi_{11}(x, s) & \phi_{12}(x, s) \\ \phi_{21}(x, s) & \phi_{22}(x, s) \end{pmatrix}, \quad (35)$$

with

$$\phi_{11} = e^{-\frac{x}{\tau \lambda_1}} e^{-\frac{x}{\lambda_1} s}, \quad (36a)$$

$$\phi_{12} = 0, \quad (36b)$$

$$\phi_{21} = \frac{\lambda_1 \left(e^{-\frac{x}{\tau \lambda_1}} e^{-\frac{x}{\lambda_1} s} - e^{-\frac{x}{\lambda_2} s} \right)}{\lambda_2 - \tau(\lambda_1 - \lambda_2)s}, \quad (36c)$$

$$\phi_{22} = e^{-\frac{x}{\lambda_2} s}. \quad (36d)$$

3.2. Free-flow case ($F > 1$)

Consider the system in the free-flow regime. From (26) we see that ζ_1 travels with characteristic speed λ_1 and ζ_2 with characteristic speed λ_2 . In the free-flow regime we have $\lambda_1 \geq \lambda_2 > 0$, hence two boundary conditions are needed, both at the upstream boundary. A plot of the characteristics is shown in Figure 1.

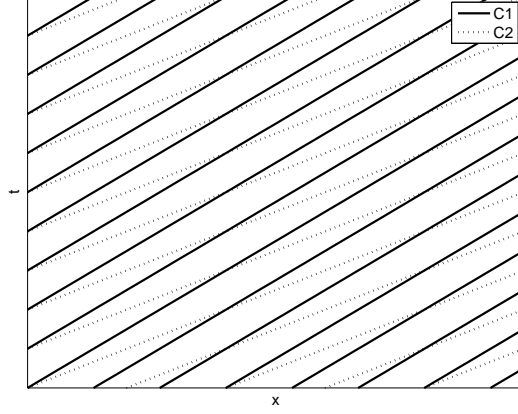


Figure 1: Illustration of the characteristics for supercritical flow, $\lambda_1 \geq \lambda_2 > 0$.

With $\zeta_1(0, t)$ and $\zeta_2(0, t)$ as the inputs and $\zeta_1(L, t)$ and $\zeta_2(L, t)$ as the outputs, the distributed transfer matrix is exactly the state-transition matrix $\Phi(x, s)$.

Using (27), we can write

$$\begin{pmatrix} \tilde{v}(x, s) \\ \tilde{q}(x, s) \end{pmatrix} = \underbrace{\begin{pmatrix} \frac{\rho^* \lambda_2}{\lambda_1 - \lambda_2} & 1 \\ \frac{\rho^* \lambda_1}{\lambda_1 - \lambda_2} & 0 \end{pmatrix}^{-1} \Phi(x, s) \begin{pmatrix} \frac{\rho^* \lambda_2}{\lambda_1 - \lambda_2} & 1 \\ \frac{\rho^* \lambda_1}{\lambda_1 - \lambda_2} & 0 \end{pmatrix}}_{\Psi(x, s)} \begin{pmatrix} \tilde{v}(0, s) \\ \tilde{q}(0, s) \end{pmatrix} \quad (37)$$

with

$$\psi_{11}(x, s) = \left(e^{-\frac{x}{\lambda_1 \tau}} e^{-\frac{x}{\lambda_1} s} - e^{-\frac{x}{\lambda_2} s} \right) \frac{\alpha}{s + \alpha} + e^{-\frac{x}{\lambda_2} s}, \quad (38a)$$

$$\psi_{12}(x, s) = -\frac{1}{\rho^* \tau} \left(e^{-\frac{x}{\lambda_1 \tau}} e^{-\frac{x}{\lambda_1} s} - e^{-\frac{x}{\lambda_2} s} \right) \frac{1}{s + \alpha}, \quad (38b)$$

$$\psi_{21}(x, s) = -\rho^* \tau \left(e^{-\frac{x}{\lambda_1 \tau}} e^{-\frac{x}{\lambda_1} s} - e^{-\frac{x}{\lambda_2} s} \right) \frac{\alpha s}{s + \alpha}, \quad (38c)$$

$$\psi_{22}(x, s) = -\left(e^{-\frac{x}{\lambda_1 \tau}} e^{-\frac{x}{\lambda_1} s} - e^{-\frac{x}{\lambda_2} s} \right) \frac{\alpha}{s + \alpha} + e^{-\frac{x}{\lambda_1 \tau}} e^{-\frac{x}{\lambda_1} s}. \quad (38d)$$

where $\alpha = -\frac{\lambda_2}{\tau(\lambda_1 - \lambda_2)}$.

3.2.1. Bode plots

We generate Bode plots using the following parameters taken from [37]: $q_{\max} = 1300$ veh/h, $\rho_{\max} = 0.1$ veh/m, and $L = 100$ m: The Greenshields Hamiltonian, $Q(\rho) = 4 \frac{q_{\max}}{\rho_{\max}^2} \rho(\rho_{\max} - \rho)$, is used to approximate the fundamental diagram. For inhomogenous second-order models, the relaxation time, τ , falls in the range of about 14-60 seconds [27]. A relaxation time of $\tau = 15$ s is used for the following simulations. We simulate for $\rho^* = 0.01$ cars \cdot m $^{-1}$.

The Bode plots for the physical variables are display in Figure 2 and Figure 3. For the Riemann invariants only $\phi_{21}(x, s)$ and $\phi_{22}(x, s)$ are represented in Figure 4 and Figure 5 ($\phi_{11}(x, s)$ and $\phi_{12}(x, s)$ are only delay functions).

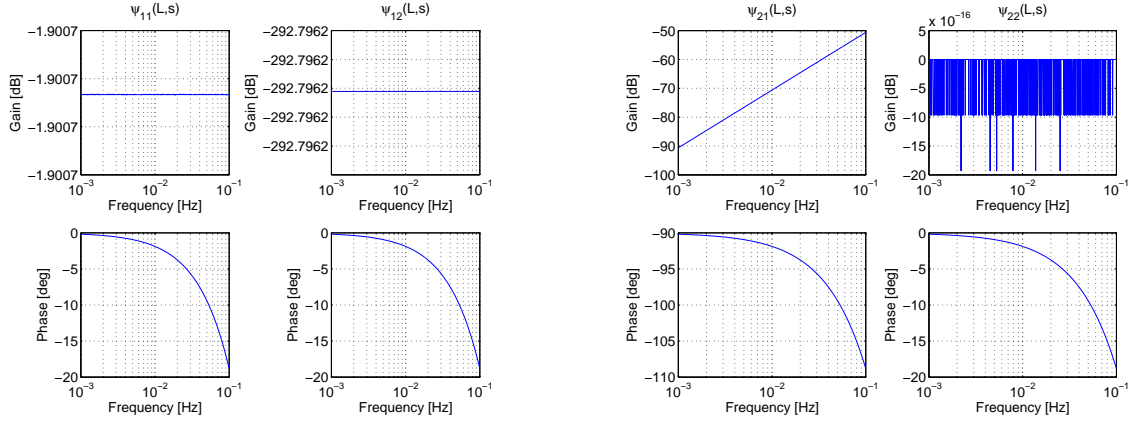


Figure 2: Magnitude and phase bode plots for $\psi_{11}(L, s)$ and $\psi_{12}(L, s)$ (left) and for $\psi_{21}(L, s)$ and $\psi_{22}(L, s)$ (right). (Physical variables).

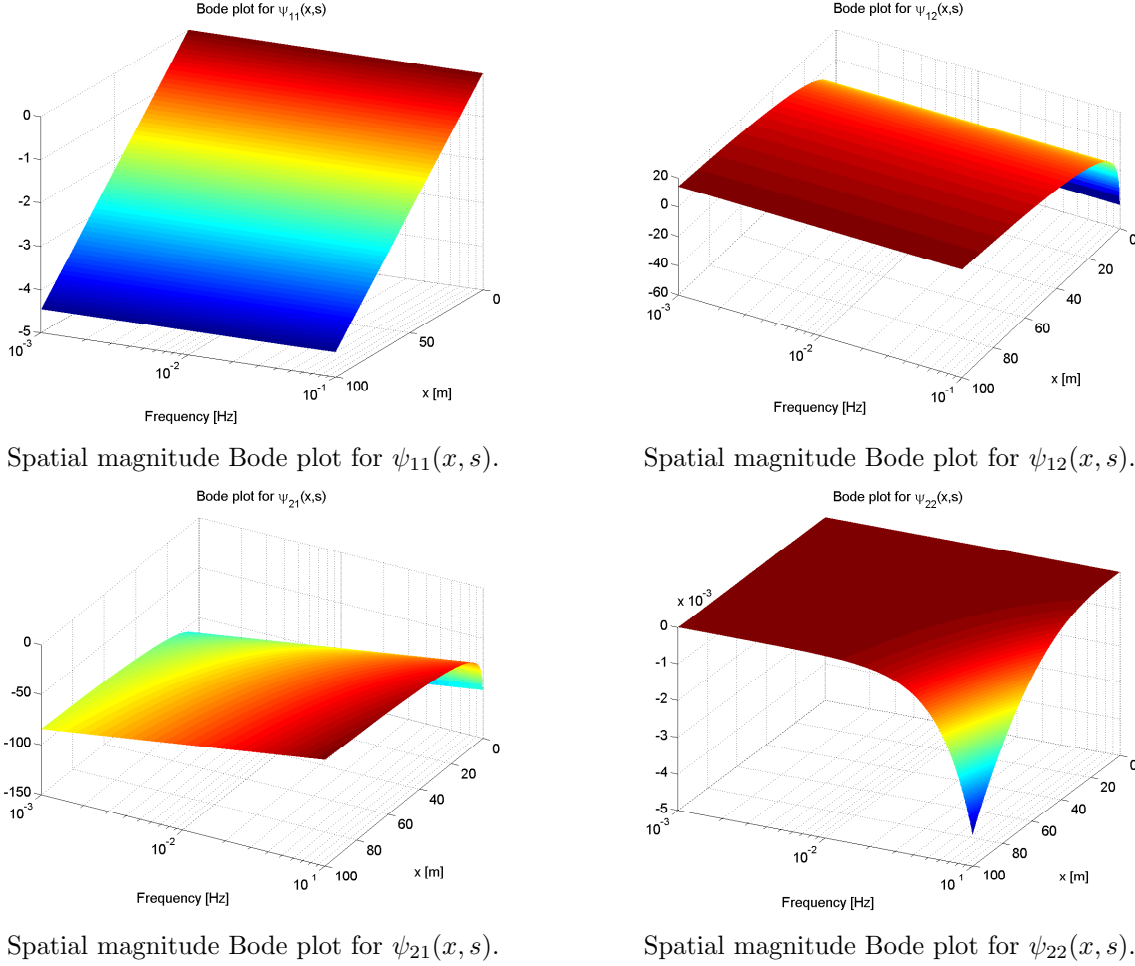
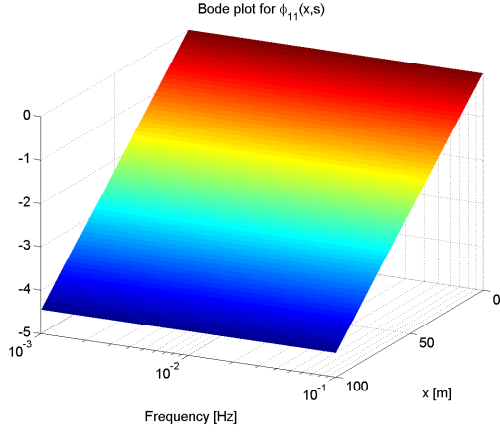
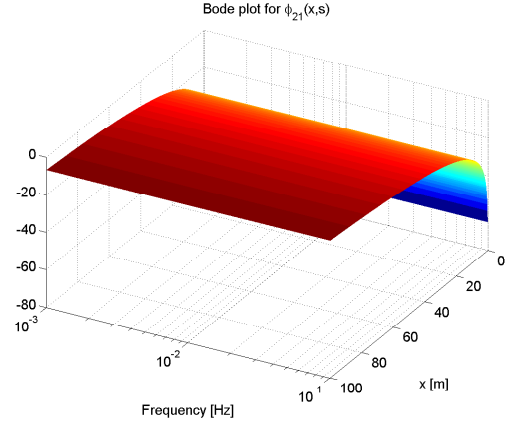


Figure 3: Spatial magnitude Bode plots for physical variables



Spatial magnitude Bode plot for $\phi_{21}(x, s)$.



Spatial magnitude Bode plot for $\phi_{22}(x, s)$.

Figure 5: Spatial magnitude Bode plots for Riemann invariants

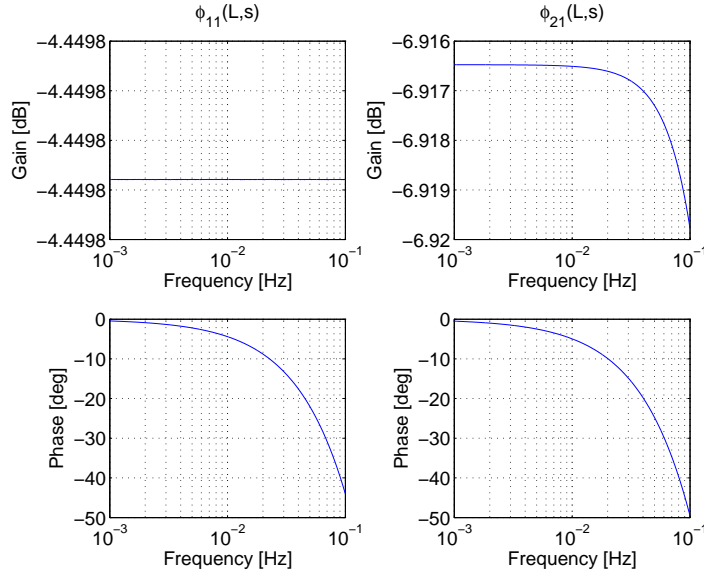


Figure 4: Magnitude and phase Bode plots for $\phi_{11}(L, s)$ and $\phi_{21}(L, s)$.

3.2.2. Step responses

We analyze the behavior of the system given step inputs $v(0, t) = v_{\text{step}}H(t)$ and $q(0, t) = q_{\text{step}}H(t)$, where $H(\cdot)$ is the Heaviside function. The step responses can be explicitly computed from the spectral responses:

$$v(x, t) = v_{\text{step}} \left[e^{-\frac{x}{\lambda_1 \tau}} \left(1 - e^{-a \left(t - \frac{x}{\lambda_1} \right)} \right) H \left(t - \frac{x}{\lambda_1} \right) + e^{-a \left(t - \frac{x}{\lambda_2} \right)} H \left(t - \frac{x}{\lambda_2} \right) \right] \\ + \frac{q_{\text{step}}}{\rho^* \tau} \left[-e^{-\frac{x}{\lambda_1 \tau}} \left(1 - e^{-a \left(t - \frac{x}{\lambda_1} \right)} \right) H \left(t - \frac{x}{\lambda_1} \right) + \left(1 - e^{-a \left(t - \frac{x}{\lambda_2} \right)} \right) H \left(t - \frac{x}{\lambda_2} \right) \right] \quad (39)$$

$$q(x, t) = v_{\text{step}} \rho^* \tau a \left[e^{-\frac{x}{\lambda_1 \tau}} e^{-a \left(t - \frac{x}{\lambda_1} \right)} H \left(t - \frac{x}{\lambda_1} \right) - e^{-a \left(t - \frac{x}{\lambda_2} \right)} H \left(t - \frac{x}{\lambda_2} \right) \right] \\ + q_{\text{step}} \left[e^{-\frac{x}{\lambda_1 \tau}} e^{-a \left(t - \frac{x}{\lambda_1} \right)} H \left(t - \frac{x}{\lambda_1} \right) + \left(1 - e^{-a \left(t - \frac{x}{\lambda_2} \right)} \right) H \left(t - \frac{x}{\lambda_2} \right) \right] \quad (40)$$

3.3. Congestion regime ($F < 1$)

We now consider the system in the congested regime. Here we have $\lambda_1 > 0, \lambda_2 < 0$, hence two boundary conditions are needed, one at the upstream boundary and one at the downstream boundary. A plot of the characteristics is shown in Figure 6.

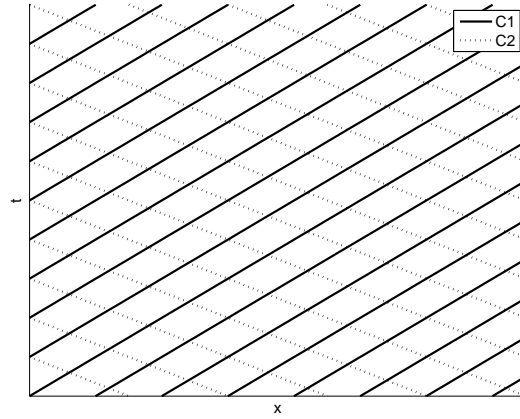


Figure 6: Illustration of the characteristics for supercritical flow, $\lambda_1 > 0, \lambda_2 < 0$.

Using (31) we can write

$$\begin{pmatrix} \hat{\xi}_1(x, s) \\ \hat{\xi}_2(x, s) \end{pmatrix} = \underbrace{\Phi(x, s) \begin{pmatrix} 1 & 0 \\ -\frac{\phi_{21}(L, s)}{\phi_{22}(L, s)} & \frac{1}{\phi_{22}} \end{pmatrix}}_{\Gamma(x, s)} \begin{pmatrix} \hat{\xi}_1(0, s) \\ \hat{\xi}_2(0, s) \end{pmatrix}. \quad (41)$$

with

$$\gamma_{11}(x, s) = e^{-\frac{x}{\lambda_1 \tau}} e^{-\frac{s x}{\lambda_1}}, \quad (42a)$$

$$\gamma_{12}(x, s) = 0, \quad (42b)$$

$$\gamma_{21}(x, s) = \alpha \frac{\lambda_1}{\lambda_2} \left(e^{-\frac{x}{\lambda_1 \tau}} e^{-\frac{s x}{\lambda_1}} - e^{-\frac{L}{\lambda_1 \tau}} e^{-\frac{s}{\lambda_2} \left(x - L \frac{\lambda_1 - \lambda_2}{\lambda_1} \right)} \right) \frac{1}{s + \alpha}, \quad (42c)$$

$$\gamma_{22}(x, s) = e^{-\frac{s(x-L)}{\lambda_2}}. \quad (42d)$$

Note that equation (41) corresponds to a closed form solution of our initial system, written in spectral form.

4. Numerical validation

Because of numerous nonlinear phenomena happening in traffic, many of them interact directly or indirectly. The linearized ARZ equations provide a finer modeling of these dynamics around a nominal operation point. The spectral form of the linearized model provides a well established theoretic framework for establishing control strategies for the system. Prior to using such techniques, it is necessary to assess how accurate the model is in its linearized form. This section compares the prediction of the model with actual flow and velocity data gathered from the well-known NGSIM data set.

4.1. Data source: NGSIM trajectories

We use the NGSIM trajectory data set for a section of the US-101 highway. The set gathers trajectories of vehicles sampled with a 10 Hz frequency thanks to high precision cameras. The data is pre-processed so as to take only cars into account; 45 minutes are recorded on a 650-meter long section with five lanes. The lanes are taken into account when computing the lineic density of vehicles ρ . The trajectories are represented in the (t, x) domain in Figure 7. Only a subset of the spatial domain is used due to the presence of ramps, which breaks the homogeneity of the freeway. The viable domain is 200 meters long.

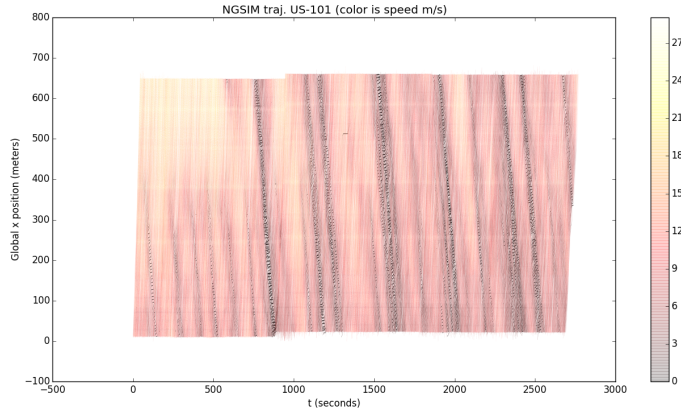


Figure 7: NGSIM trajectories. Color represents the measured speed of each car in m/s.

4.2. Reconstructing (v, q) maps from NGSIM trajectories

The NGSIM data set does not directly provide the values $v(t, x)$ and $q(t, x)$ in the resolution domain $[0, T] \times [0, L]$. In order to obtain macroscopic quantities out of the microscopic measurements, we divide the space-time grid into cells $([i\Delta t, (i+1)\Delta t] \times [j\Delta x, (j+1)\Delta x])_{i \in \{1 \dots n_t\}, j \in \{1 \dots n_x\}}$, where n_t and n_x are the number of cells in time and space, respectively. This operation consists of gathering corresponding data points into cells, then estimating the quantities of interest in each cell.

The size of each cell is $\Delta t \times \Delta x$. Within each cell, a specific number of traces, or footprints of a vehicle along its trajectory, are available, and ρ , v , and q are assumed to be constant. We present several formulae to map a set of traces to speed, flow, and density over the space-time grid.

Binning formula for v : Since the speed is assumed to be constant in each cell, a straightforward estimate for the speed is the empirical average. Let $\hat{v}_{i,j}$ be the estimator for the speed in cell (i, j) :

$$\hat{v}_{i,j} = \text{mean}_{\text{trace} \in \text{bin}_{i,j}}(v(\text{trace})) \quad (43)$$

Binning formula for ρ : Consider a cell with index (i, j) . By definition,

$$\rho_{i,j} = \frac{1}{n_{\text{lanes}} \Delta x \Delta t} \iint_{(t,x) \in [i\Delta t, (i+1)\Delta t] \times [j\Delta x, (j+1)\Delta t]} \rho(x, t) dx dt. \quad (44)$$

The position of each vehicle is recorded every 0.1 second. We count the number of traces in a given cell and normalize it by the sampling rate. The contribution of a given vehicle to the density of a cell is

proportional to the number of traces it has left in the cell. If the speed is assumed to be locally constant, this contribution is proportional to the time this vehicle spends in the cell and is consistent with the conservation of the total number of vehicles across all cells.

$$\hat{\rho}_{i,j} = \frac{1}{n_{\text{lanes}} \Delta x \Delta t \text{ sampling rate}} \text{card}(\{\text{trace} \mid \text{trace} \in \text{bin}\}), \quad (45)$$

where $\text{card}(\cdot)$ gives the number of elements in a set, i.e., its cardinal.

Binning formula for q :

By definition, $q(x, t) = \rho(x, t) v(x, t)$, so a logical first estimate for q in cell (i, j) is

$$\hat{q}_{i,j} = \hat{v}_{i,j} \hat{\rho}_{i,j}. \quad (46)$$

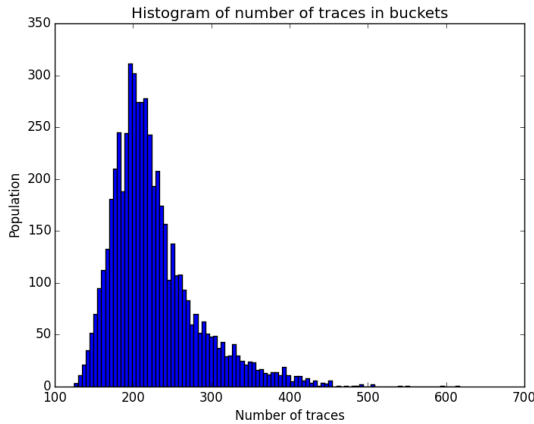
We can also approximate the flux going through a given cell $[i \Delta t, (i+1) \Delta t] \times [j \Delta x, (j+1) \Delta t]$ by the number of cars crossing the x coordinate $(j+1) \Delta x$ between times $i \Delta t$ and $(i+1) \Delta t$ normalized by the duration Δt .

If a given vehicle with identification number id crosses $(j+1) \Delta x$ between time $i \Delta t$ and time $(i+1) \Delta t$, then id is present in bins $[i \Delta t, (i+1) \Delta t] \times [j \Delta x, (j+1) \Delta t]$ and $[i \Delta t, (i+1) \Delta t] \times [(j+1) \Delta x, (j+2) \Delta t]$. Therefore, $\text{card}(\{\text{id}(\text{trace}) \mid \text{trace} \in \text{bin}_{i,j}\} \cap \{\text{id}(\text{trace}) \mid \text{trace} \in \text{bin}_{i,j+1}\})$ is the number of vehicles that have crossed the coordinate $(j+1) \Delta x$ in that interval of time. This gives another estimator of the flux based on counting cars in a straightforward way:

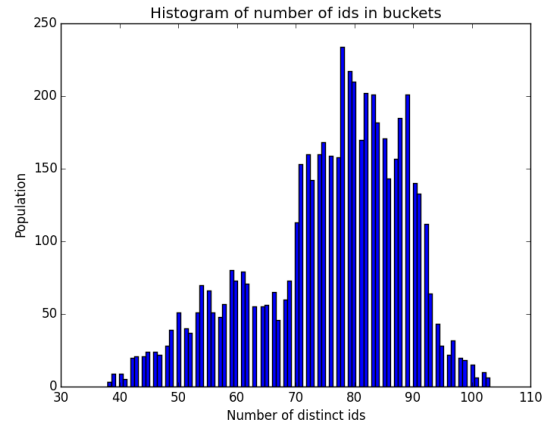
$$\hat{q}_{i,j}^{\text{count}} = \frac{1}{n_{\text{lanes}} \Delta t} \text{card}(\{\text{id}(\text{trace}) \mid \text{trace} \in \text{bin}_{i,j}\} \cap \{\text{id}(\text{trace}) \mid \text{trace} \in \text{bin}_{i,j+1}\})$$

4.2.1. Choosing the number of bins

The discretization grid is $\{[i \Delta t, (i+1) \Delta t] \times [j \Delta x, (j+1) \Delta t] \mid (i, j) \in \{1 \dots N\} \times \{1 \dots N\}\}$. As the estimation formulae above rely on averaging, having a comfortable number of points in each bin provides more stable estimates. It is worth mentioning that usual central limit theorem based reasoning for convergence of such estimates is flawed as several samples may correspond to the same vehicle or interacting vehicles, therefore violating the independence assumption of the theorem. Proving the convergence of the estimates above lies clearly beyond the scope of this article and therefore, as a rule of thumb we choose a setup that guarantees that most bins will host more than 100 traces. This is achieved with a 80×80 grid where the 10th percentile of the number of traces in a given bin is 170. Such a grid also yields a 10th percentile of 56 distinct vehicles per bin. The histograms of number of traces and vehicle per cell are represented in Figure 8.



Histogram of number of traces per cell.



Histogram of number of distinct vehicles per cell.

Figure 8: Experimental justification for a 80×80 cell based discretization grid for the NGSIM data.

While it is not the goal of the present article to present theoretical proofs of the convergence of the binned estimators for (v, ρ, q) , it is nonetheless possible to check practically that the procedure is coherent. Two estimators are provided for q that use radically different techniques. The first one relies on the average measured speed and the number of traces in a bin. The other one on counting vehicles transiting from a cell to another. Verifying that they both give similar results for a given cell will therefore confirm that these estimators for q are trustworthy. It will also certify that the estimation technique for ρ is valid. As one can observe in Figure 13, the scatter plot of $\hat{q}_{i,j}^{\text{count}}$ is plotted against $\hat{q}_{i,j}$ coincides almost perfectly with the line $y = x$ therefore validating the overall binning and estimation procedure.

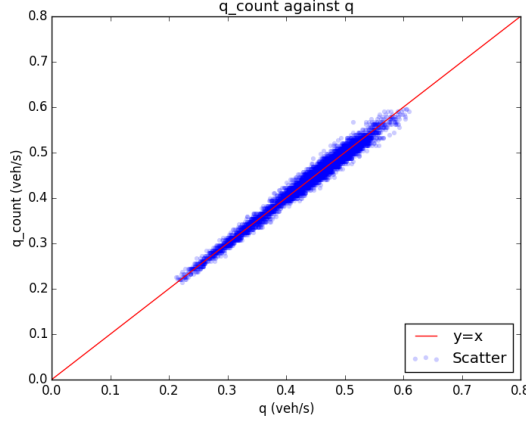


Figure 9: Sanity check for the estimation procedure. $\hat{q}_{i,j}^{\text{count}}$ is plotted against $\hat{q}_{i,j}$ across the grid of bins.

4.3. Estimated values for (v, q)

In order to check how well the linearized ARZ model fits actual data, we chose a bounded domain and compares the theoretical solution given by the second order model and the observed data. Here we focus on the values of v and q as they correspond to the setup that is the most worth studying. It is also the most directly practical for control. Now that estimates of the actual values of v and q have been designed, they will be used to compute fundamental diagrams and mapped on the $[0, T] \times [0, L]$ domain. Fundamental diagrams will then yield estimates of the eigen values λ_1 and λ_2 that are crucial in this study. Finally, predicted values of v and q will be compared to their measured counterparts which will allow the computation of a fit error. Based on the estimation of this error for different values of the parameter τ , the value offering the best fit will be used as an estimate. Plotting maps of both the predicted values and the observed one will also highlight the phenomena the linearized model accounts for and those it cannot characterize.

Maps. Once the values $\hat{v}_{i,j}$, $\hat{\rho}_{i,j}$, $\hat{q}_{i,j}$, $\hat{q}_{i,j}^{\text{count}}$ have been computed they can be plotted on the discretization grid (see Figure 10). As \hat{q} and \hat{q}^{count} give extremely similar results, \hat{q}^{count} will be used as the estimator of q from now on. Damped oscillations and smoothly decaying values along characteristic lines are the main characteristic the practical implementation of the model should feature.

Fundamental diagrams. From the values that have been estimated it is very straightforward to compute fundamental diagrams as in Figure 11. One of the potential flaws of studying these fundamental diagrams and using them to calibrate the model's parameters as we do below could come from the fact that the dataset is small. Even though many points are collected, they only give information about cars traveling in a small region of time and space. Therefore it is certain that our measurements are highly correlated. This seems to be confirmed by the fact that the fundamental diagrams below only correspond to the congested regime. *OPTIONAL: Most of the points are concentrated about the same region. This is not enough to guarantee that the estimated quantities are reliable. However, NGSIM is to this day one of the most comprehensive data sets of vehicle behavior on a freeway. It is therefore one of the best ways one has to validate that a traffic model is realistic. The fact that most points lie in the same region is also a sign that the linearization hypothesis is reasonable in that context. Observed deviations from the equilibrium are indeed generally small. (The equilibrium, i.e. the linearization point, is estimated below).*

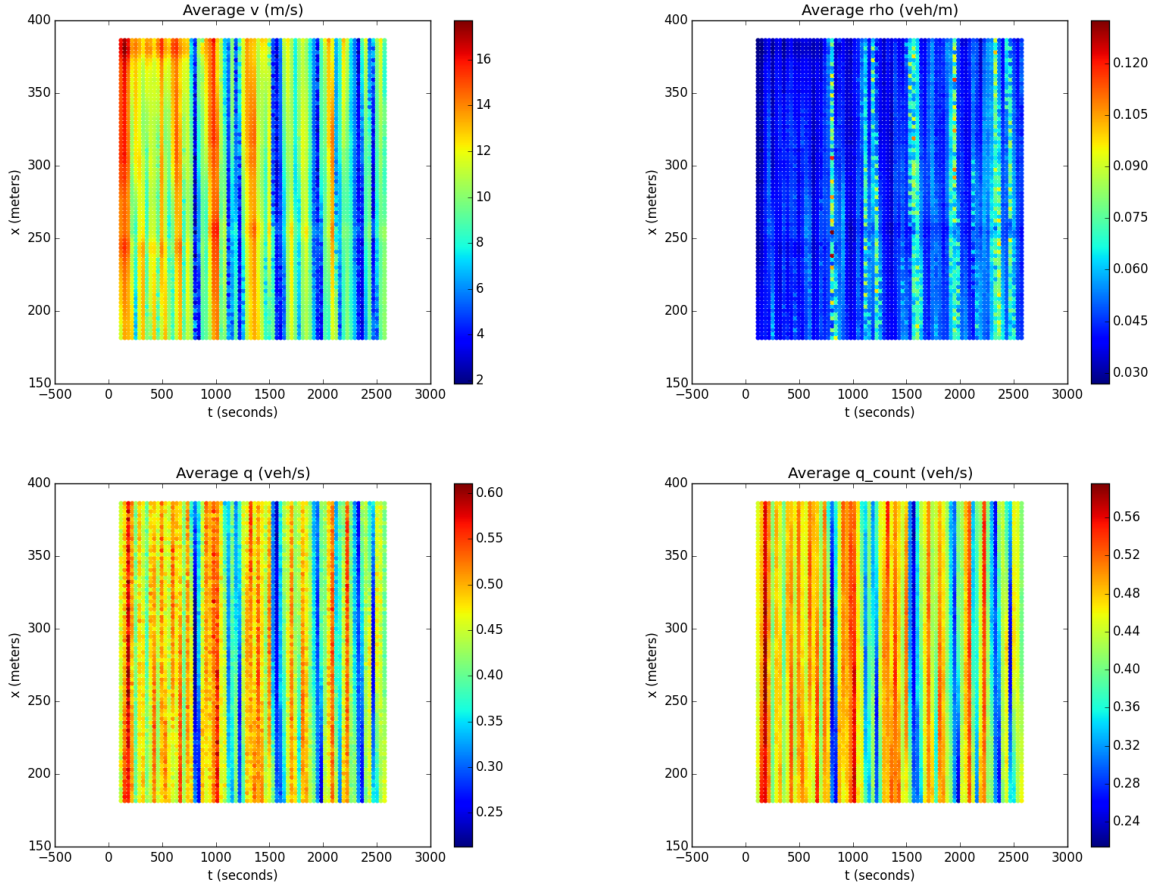


Figure 10: Estimated values for (v, q, ρ) . Top left: $\hat{v}_{i,j}$. Top right: $\hat{\rho}_{i,j}$. Bottom left: $\hat{q}_{i,j}$. Bottom right: $\hat{q}_{i,j}^{\text{count}}$.

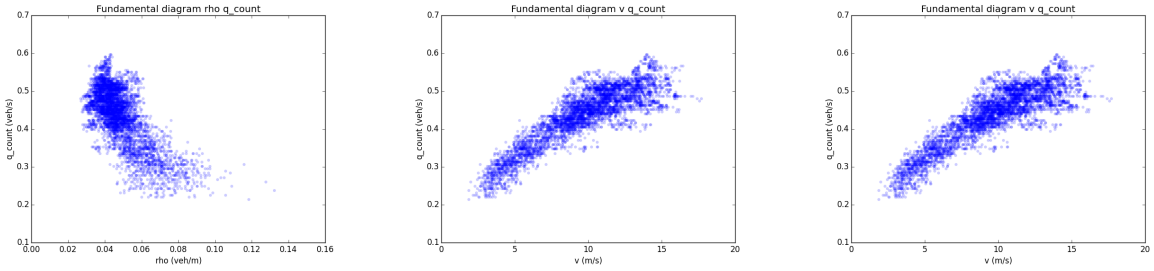


Figure 11: Empirical fundamental diagrams. Left: $(\hat{\rho}, \hat{q}^{\text{count}})$. Middle: $(\hat{v}, \hat{q}^{\text{count}})$. Right: $(\hat{\rho}, \hat{v})$.

4.3.1. Calibration of λ_1 and λ_2 , linearization point

From section 2, $\lambda_1 = v^*$ and $\lambda_2 = Q'(v^*)$, therefore the calibration of λ_1 consists in finding a value of v around which the fundamental diagram (v, q) will be linearized. By definition, λ_2 corresponds to the slope of the fundamental diagram. It is estimated in practice thanks to a standard Ordinary Least Squares method. The data set above only corresponds to the congested regime and the fundamental diagram is almost affine.

The method used here is the following. The estimator for v^* is chosen as the empirical mean of $\hat{v}_{i,j}$: $\hat{\lambda}_1 = \hat{v}^*$. A linear model is fitted: $\hat{q}^{\text{count}} = b_1 \hat{v} + b_0 + \varepsilon$ (where ε represents the noise in the model that would ideally be centered, homoschedastic and uncorrelated but is not practically) and the estimator for λ_2 is then

$\hat{\lambda}_2 = \hat{b}_1$. q^* is estimated by the empirical average of \hat{q}^{count} and ρ^* by the ratio of the estimates for q^* and v^* . Provided each estimator is convergent, the continuity of the functional $(x, y) \rightarrow \frac{x}{y}$ on its domain guarantees the convergence of the estimator for ρ^* . The empirical results are presented in Figure 12. The determination coefficient is poor, it could be improved by filtering out outliers and more generally by gathering more data. Improving the quality of the estimation will be the subject of further work on that matter. Significance tests for the coefficients of the linear model are not presented. The assumptions they rely on about the linear dependency between \hat{q} and \hat{v} are clearly not respected here as the noise is auto-correlated. Further work needs to turn this rather heuristic method for estimating parameters into a fully justified statistical procedure. This article focuses is qualitatively assessing what phenomena can be accounted for by the linearized second order model.

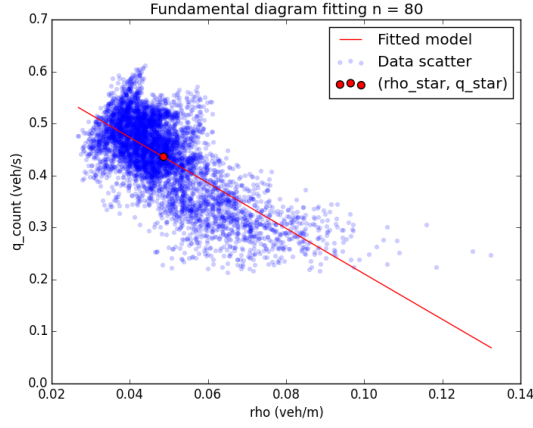


Figure 12: Calibration of λ_1 and λ_2 . The figure shows the average point used to compute \hat{v}^* and \hat{q}^* . The affine model used to estimate λ_2 is also plotted. $\hat{\lambda}_1 = 8.96$, $\hat{\lambda}_2 = -4.37$, $\hat{\rho}^* = 0.049$, $\hat{v}^* = 8.96$, $\hat{q}^* = 0.44$, $r^2 = 0.48$

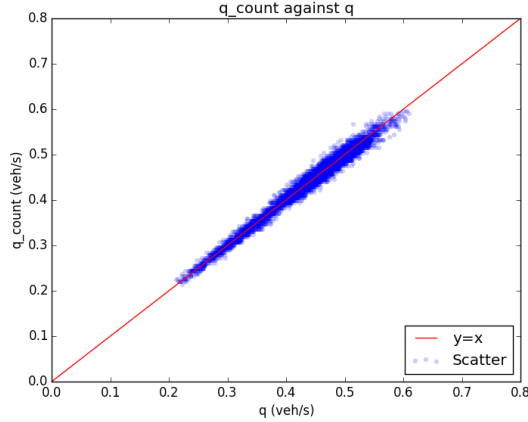


Figure 13: Sanity check for the estimation procedure. $\hat{q}_{i,j}^{\text{count}}$ is plotted against $\hat{q}_{i,j}$ across the grid of bins.

4.4. Simulated values for (v, q, ρ)

The data above shows that only the congested regime is to be modeled for the NGSIM data. Therefore the theory developed for the $\lambda_2 < 0$ will be put to use here.

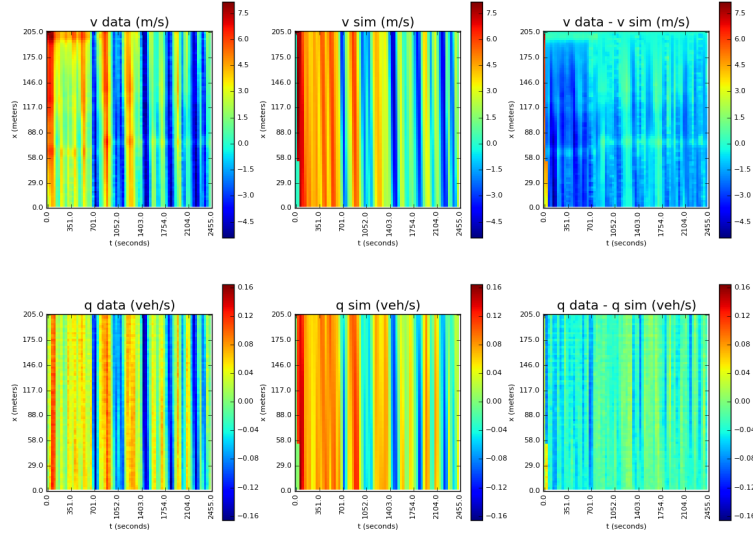
4.4.1. Fourier decomposition of input for a linear PDE

The Partial Differential Equation under scrutiny here is linearized. Therefore, decomposing boundary conditions into a sum and then adding the predicted values inside the domain $[0, T] \times [0, L]$ will give the

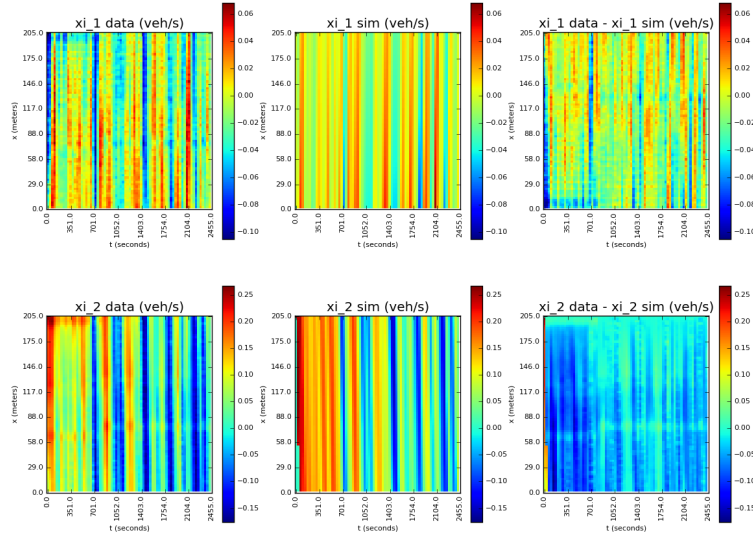
exact solution. The spectral domain analysis presented above is very useful to that end and will be leveraged thanks to Fourier analysis. Fourier transform is a linear operator that is practically implemented thanks to the Fast Fourier Transform. A real signal $\{f(t) \mid t \in [0, T]\}$ on one of the boundaries $\{(x = 0, t) \mid t \in [0, T]\}$ or $\{(x = L, t) \mid t \in [0, T]\}$ is transformed into a periodic signal by infinite duplication and then turned into a Fourier series $\{t \rightarrow \mu + \sum_{k=1}^n \beta_k \cdot \cos(k \cdot wt + \phi_k) H \mid t \in [0, T]\}$. This process is known to be convergent with an infinite sum for any square integrable function. It is practically extremely accurate in our case even though the FFT only relies on a finite number of Fourier coefficients. For both upstream and downstream boundary conditions, eye inspection cannot distinguish the original signal from its Fourier series decomposition. In Appendix 4.5 the generic way of computing the solution of the PDE inside the inner domain is presented. The process is quite straightforward although the necessary computations are somewhat cumbersome.

4.4.2. Simulated maps

Prior to using Fourier decomposed signals and elementary solutions, it is necessary to convert the data into the diagonalized basis. First of all, the difference with respect to the equilibrium is computed for each bin: $\widehat{v}_{i,j} = \widehat{v}_{i,j} - \widehat{v}^*$, $\widehat{q}_{i,j} = \widehat{q}_{i,j} - \widehat{q}^*$. Once λ_1 and λ_2 have been estimated, estimates for ξ_1 and ξ_2 are computed thanks to the following equations: $\widehat{\xi}_{1,i,j} = \frac{\widehat{\rho}^* \widehat{\lambda}_2}{\lambda_1 - \lambda_2} \widehat{v}_{i,j} + \widehat{q}_{i,j}$, $\widehat{\xi}_{2,i,j} = \frac{\widehat{\rho}^* \widehat{\lambda}_1}{\lambda_1 - \lambda_2} \widehat{v}_{i,j}$. Then the predicted values for q and v can be computed thanks to the inverse linear transform $\widetilde{q} = \xi_1 - \frac{\lambda_1}{\lambda_2} \xi_2$, $\widetilde{v} = \frac{\lambda_1 - \lambda_2}{\rho^* \lambda_1} \xi_2$. This procedure gives comparison maps for the data and predicted values for both the (v, q) and the (ξ_1, ξ_2) domains. Figure 14 shows important qualitative properties of the model. First of all, as expected, the model generally predicts with a very good accuracy the decay of all quantities along their characteristic lines. This is a realistic feature that cannot be paralleled by first order models. The general quality of the fit is rather good with most of the error on v and q in a 20 percent range of the data's amplitude between minimum and maximum values. What is also quite satisfactory is that the linearized second order model manages to capture oscillations observed on the boundary and account for their decay accurately. The value of τ used to compute the plots below is described in 4.4.3.



Top row: q . Bottom row: v .



Top row: ξ_1 . Bottom row: ξ_2 .

Figure 14: Data versus predicted. Top: (v, q) domain. Bottom: (ξ_1, ξ_2) domain. First column: data. Middle column: predictions. Third column: prediction - data.

4.4.3. Calibration of τ

For each value of τ one computes the mean absolute error (MAE). That is to say, the average difference in absolute value between what is simulated and what is predicted for each discretization bin. v and q are not physically homogeneous, therefore it is not sensible to aggregate the errors over these quantities. However, ξ_1 and ξ_2 are both expressed in veh/s. Summing their MAE gives a reliable uni-dimensional index of the quality of the fit with respect to τ . This quantity is computed for different values of τ ranging from 5 to 80 seconds. The value offering the best fit is $\tau^* = 39.18$.

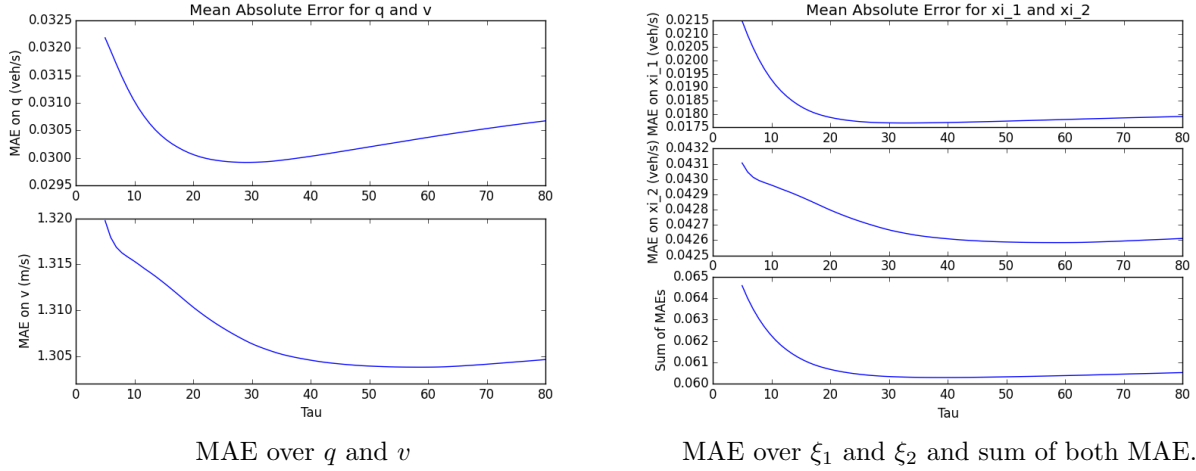


Figure 15: Calibration of τ , one minimizes the sum of MAE over ξ_1 and ξ_2 .

4.5. Generic computations for time domain to Laplace domain transforms and vice versa

The aim is to derive the time domain responses of generic input signals such as $t \rightarrow H(t)$ and $t \rightarrow \cos(\omega t + \phi) H(t)$ when multiplied in the Laplace domain by $\frac{1}{s+\alpha}$. This then enables the computation of any response that decomposes in a Fourier transform.

4.5.1. Step function input

The time domain input function is $H(t)$. One computes the inverse Laplace transform of $s \rightarrow \frac{1}{s(s+\alpha)}$ which is

$$t \rightarrow \frac{1}{\alpha} (1 - e^{-\alpha t}) H(t)$$

4.5.2. Phased cosine input

The time domain input function is $\cos(\omega t + \phi) H(t)$. One computes the inverse Laplace transform of $s \rightarrow \frac{1}{s+\alpha} \left\{ \frac{s}{s^2+\omega^2} \cos(\phi) - \frac{\omega}{s^2+\omega^2} \sin(\phi) \right\}$ which can be directly achieved in the time domain. Indeed, the result is given by the convolution product $t \rightarrow (e^{-\alpha \cdot} H(\cdot) \star \cos(\omega \cdot + \phi) H(\cdot))(t)$, that is to say

$$t \rightarrow \frac{-e^{-\alpha t} (\alpha \cdot \cos(\phi) + \omega \cdot \sin(\phi)) + \alpha \cdot \cos(\omega t + \phi) + \omega \cdot \sin(\omega t + \phi)}{\alpha^2 + \omega^2} H(t) = \kappa_{\alpha, \omega, \phi}^{\cos}(t)$$

4.5.3. Fourier sum input

Let the input be $t \rightarrow \mu H(t) + \sum_{k=1}^n \beta_k \cdot \cos(k \cdot \omega t + \phi_k) H(t)$. The time domain response is therefore

$$t \rightarrow \frac{\mu}{\alpha} (1 - e^{-\alpha t}) H(t) + \sum_{k=1}^n \beta_k \cdot \kappa_{\alpha, \omega, \phi}^{\cos}(t)$$

4.6. Fourier decomposition and time domain responses for $\lambda_2 > 0$

Let $\alpha = -\frac{\lambda_2}{\tau(\lambda_1 - \lambda_2)} < 0$. Let $H(t)$ the Heaviside function.

$$\begin{pmatrix} \hat{\xi}_1(x, s) \\ \hat{\xi}_2(x, s) \end{pmatrix} = \Phi(x, s) \begin{pmatrix} \hat{\xi}_1(0, s) \\ \hat{\xi}_2(0, s) \end{pmatrix}$$

with

$$\Phi(x, s) = \begin{bmatrix} e^{-\frac{s x}{\lambda_1}} e^{-\frac{x}{\lambda_1 \tau}} & 0 \\ -\alpha \frac{\lambda_1}{\lambda_2} \left(e^{-\frac{s x}{\lambda_1}} e^{-\frac{x}{\lambda_1 \tau}} - e^{-\frac{s x}{\lambda_2}} \right) \frac{1}{s+\alpha} & e^{-\frac{s x}{\lambda_2}} \end{bmatrix}$$

implies the following fundamental responses for the system.

4.6.1. Fundamental responses in time domain:

- $\begin{pmatrix} \xi_1(0, t) \\ \xi_2(0, t) \end{pmatrix} = \begin{pmatrix} H(t) \\ 0 \end{pmatrix}$:
 - $\xi_1(x, t) = e^{-\frac{x}{\lambda_1 \tau}} H\left(t - \frac{x}{\lambda_1}\right)$
 - $\xi_2(x, t) = -\frac{\lambda_1}{\lambda_2} \left(e^{-\frac{x}{\lambda_1 \tau}} \left(1 - e^{-\alpha\left(t - \frac{x}{\lambda_1}\right)}\right) H\left(t - \frac{x}{\lambda_1}\right) - \left(1 - e^{-\alpha\left(t - \frac{x}{\lambda_2}\right)}\right) H\left(t - \frac{x}{\lambda_2}\right) \right)$
- $\begin{pmatrix} \xi_1(0, t) \\ \xi_2(0, t) \end{pmatrix} = \begin{pmatrix} 0 \\ H(t) \end{pmatrix}$:
 - $\xi_1(x, t) = 0$
 - $\xi_2(x, t) = H\left(t - \frac{x}{\lambda_2}\right)$
- $\begin{pmatrix} \xi_1(0, t) \\ \xi_2(0, t) \end{pmatrix} = \begin{pmatrix} \cos(\omega t + \phi) \\ 0 \end{pmatrix}$:
 - $\xi_1(x, t) = e^{-\frac{x}{\lambda_1 \tau}} \cos\left(\omega\left(t - \frac{x}{\lambda_1}\right) + \phi\right) H\left(t - \frac{x}{\lambda_1}\right)$
 - $\xi_2(x, t) = -\frac{\lambda_1 \alpha}{\lambda_2} \left(e^{-\frac{x}{\lambda_1 \tau}} \kappa_{\alpha, \omega, \phi}^{\cos}\left(t - \frac{x}{\lambda_1}\right) - \kappa_{\alpha, \omega, \phi}^{\cos}\left(t - \frac{x}{\lambda_2}\right) \right)$
- $\begin{pmatrix} \xi_1(0, t) \\ \xi_2(0, t) \end{pmatrix} = \begin{pmatrix} 0 \\ \cos(\omega t + \phi) \end{pmatrix}$:
 - $\xi_1(x, t) = 0$
 - $\xi_2(x, t) = \cos\left(\omega\left(t - \frac{x}{\lambda_2}\right) + \phi\right) H\left(t - \frac{x}{\lambda_2}\right)$

4.7. Fourier decomposition and time domain responses for $\lambda_2 < 0$

This time, $\alpha = -\frac{\lambda_2}{\tau(\lambda_1 - \lambda_2)} > 0$.

$$\begin{pmatrix} \hat{\xi}_1(x, s) \\ \hat{\xi}_2(x, s) \end{pmatrix} = \Phi(x, s) \begin{pmatrix} \hat{\xi}_1(0, s) \\ \hat{\xi}_2(L, s) \end{pmatrix}$$

with

$$\Gamma(x, s) = \begin{pmatrix} e^{-\frac{s x}{\lambda_1}} e^{-\frac{x}{\lambda_1 \tau}} & 0 \\ \alpha \frac{\lambda_1}{\lambda_2} \left(e^{-\frac{x}{\lambda_1 \tau}} e^{-\frac{s x}{\lambda_1}} - e^{-\frac{L}{\lambda_1 \tau}} e^{-\frac{s}{\lambda_2} \left(x - L \frac{\lambda_1 - \lambda_2}{\lambda_1}\right)} \right) \frac{1}{s + \alpha} & e^{-\frac{s(x-L)}{\lambda_2}} \end{pmatrix}$$

implies the following fundamental responses for the system.

4.7.1. Fundamental responses in time domain

- $\begin{pmatrix} \xi_1(0, t) \\ \xi_2(L, t) \end{pmatrix} = \begin{pmatrix} H(t) \\ 0 \end{pmatrix}$:
 - $\xi_1(x, t) = e^{-\frac{x}{\lambda_1 \tau}} H\left(t - \frac{x}{\lambda_1}\right)$
 - $\xi_2(x, t) = \frac{\lambda_1}{\lambda_2} \left(e^{-\frac{x}{\lambda_1 \tau}} \left(1 - e^{-\alpha\left(t - \frac{x}{\lambda_1}\right)}\right) H\left(t - \frac{x}{\lambda_1}\right) - e^{-\frac{L}{\lambda_1 \tau}} \left(1 - e^{-\alpha\left(t - \frac{x-L}{\lambda_2}\right)}\right) H\left(t - \frac{x-L}{\lambda_2}\right) \right)$

- $\begin{pmatrix} \xi_1(0, t) \\ \xi_2(L, t) \end{pmatrix} = \begin{pmatrix} 0 \\ H(t) \end{pmatrix}$:
 - $\xi_1(x, t) = 0$
 - $\xi_2(x, t) = H\left(t - \frac{x-L}{\lambda_2}\right)$
- $\begin{pmatrix} \xi_1(0, t) \\ \xi_2(L, t) \end{pmatrix} = \begin{pmatrix} \cos(\omega t + \phi) \\ 0 \end{pmatrix}$:
 - $\xi_1(x, t) = e^{-\frac{x}{\lambda_1 \tau}} \cos\left(\omega\left(t - \frac{x}{\lambda_1}\right) + \phi\right) H\left(t - \frac{x}{\lambda_1}\right)$
 - $\xi_2(x, t) = \frac{\lambda_1 \alpha}{\lambda_2} \left(e^{-\frac{x}{\lambda_1 \tau}} \kappa_{\alpha, \omega, \phi}^{\cos}\left(t - \frac{x}{\lambda_1}\right) - e^{-\frac{L}{\lambda_1 \tau}} \kappa_{\alpha, \omega, \phi}^{\cos}\left(t - \frac{x-L \frac{\lambda_1 - \lambda_2}{\lambda_1}}{\lambda_2}\right) \right)$
- $\begin{pmatrix} \xi_1(0, t) \\ \xi_2(L, t) \end{pmatrix} = \begin{pmatrix} 0 \\ \cos(\omega t + \phi) \end{pmatrix}$:
 - $\xi_1(x, t) = 0$
 - $\xi_2(x, t) = \cos\left(\omega\left(t - \frac{x-L}{\lambda_2}\right) + \phi\right) H\left(t - \frac{x-L}{\lambda_2}\right)$

5. Conclusion

In this article we have shown how to use linearization of second order traffic model so as to characterize important properties of the system such as Riemann Invariants. In particular time domain responses predict in the free-flow regime that the system is unstable and traffic waves would see their amplitude increase at an exponential rate before the system drifts away from the equilibrium point. This is a strong result that sheds a new light on traffic oscillations. In the congested regime such oscillatory phenomena are also present as we have shown in our numerical experiments. The new method of analysis and its spectral form will later on make any control strategy easy to set up. The higher realism of the ARZ model as compared to LWR will enable efficient traffic regulation on freeways thank to varying speed limits and on-ramp metering. It will also avoid resonating with jamitons. Further work needs to focus on designing such traffic optimization schemes. Numerically, new methods for macroscopic variable estimation have been developed that are reliable practically. Although it is still necessary to prove the convergence of this estimation procedure and which resolution should be used for such tasks. It is interesting to see that, thanks to the spectral resolution of the problem, the choice of the grid size is then driven by statistical convergence and not by CFL conditions.

Acknowledgments

References

- [1] M. J. Lighthill, J. B. Whitham, On kinematic waves. II: A theory of traffic flow on long crowded roads., Proc. Royal. Soc. (1955) 317–345.
- [2] P. I. Richards, Shock waves on the highway, Operations Research 4 (1) (1956) 42–51.
- [3] B. D. Greenshields, A study of traffic capacity, in: Highway Research Board Proceedings, 1934, pp. 448–474.
- [4] H. Greenberg, An analysis of traffic flow, Operations Research.
- [5] G. F. Newell, A simplified theory of kinematic waves in highway traffic, part II: queueing at freeway bottlenecks, Transp. Res. Part B 27 (7) (1993) 289–303.
- [6] C. F. Daganzo, The cell transmission model: A dynamic representation of highway traffic consistent with the hydrodynamic theory, Transp. Res. Part B 28 (4) (1994) 269–287.

- [7] Y. Wang, M. Papageorgiou, Real-time freeway traffic state estimation based on extended kalman filter: a general approach, *Transportation Research Part B: Methodological* 39 (2) (2005) 141 – 167. doi: <http://dx.doi.org/10.1016/j.trb.2004.03.003>.
URL <http://www.sciencedirect.com/science/article/pii/S0191261504000438>
- [8] M. Papageorgiou, J.-M. Blosseville, H. Hadj-Salem, Macroscopic modelling of traffic flow on the boulevard priphrique in paris, *Transportation Research Part B: Methodological* 23 (1) (1989) 29 – 47. doi: [http://dx.doi.org/10.1016/0191-2615\(89\)90021-0](http://dx.doi.org/10.1016/0191-2615(89)90021-0).
URL <http://www.sciencedirect.com/science/article/pii/0191261589900210>
- [9] S. K. Godunov, A difference scheme for numerical solution of discontinuous solution of hydrodynamic equations, *Math. Sbornik* 47 (1969) 271–306.
- [10] S. Osher, Riemann solvers, the entropy condition, and difference, *SIAM Journal on Numerical Analysis* 21 (2) (1984) 217–235.
- [11] C. F. Daganzo, The cell transmission model, part ii: network traffic, *Transp. Res. Part B* 29 (2) (1995) 79–93.
- [12] C. F. Daganzo, Requiem for second-order fluid approximations of traffic flow, *Transp. Res. Part B* 29 (4) (1995) 277–286.
- [13] Y. Sugiyama, M. Fukui, M. Kikuchi, K. Hasebe, A. Nakayama, K. Nishinari, S. ichi Tadaki, S. Yukawa, Traffic jams without bottlenecks, experimental evidence for the physical mechanism of the formation of a jam, *New J. Phys.*
- [14] M. R. Flynn, A. R. Kasimov, J. c. Nave, R. R. Rosales, B. Seibold, On ?jamitons, ? self-sustained nonlinear traffic waves (2008).
- [15] M. R. Flynn, A. R. Kasimov, J. c. Nave, R. R. Rosales, B. Seibold, Self-sustained nonlinear waves in traffic flow, *Physical Review E* 79 (2009) 056113.
- [16] B. Seibold, M. R. Flynn, A. R. Kasimov, R. R. Rosales, Constructing set-valued fundamental diagrams from jamiton solutions in second order traffic models, *ArXiv e-prints* [arXiv:1204.5510](https://arxiv.org/abs/1204.5510).
- [17] H. J. Payne, *Models of Freeway Traffic and Control*, Simulation Councils, Incorporated, 1971.
- [18] G. B. Whitham, *Linear and Nonlinear Waves*, A Wiley-Interscience publication, Wiley, 1974.
- [19] G. F. Newell, Nonlinear effects in the dynamics of car following, *Operations Research* 9 (2) (1961) 209–229.
- [20] H. M. Zhang, A non-equilibrium traffic model devoid of gas-like behavior, *Transp. Res. Part B* 36 (2002) 275–290.
- [21] H. M. Zhang, A theory of nonequilibrium traffic flow, *Transp. Res. Part B* 32 (7) (1998) 485–498.
- [22] A. Aw, M. Rascle, Resurrection of second order models of traffic flow, *SIAM Journal of Applied Mathematics* 60 (3) (2000) 916–938.
- [23] M. Rascle, An improved macroscopic model of traffic flow: derivation and links with the lighthill-whitham model, *Mathematical and computer modelling* 35 (2002) 581–590.
- [24] J.-P. Lebacque, S. Mammar, H. Haj-Salem, The aw-rasclé and zhang’s model: Vacuum problems, existence and regularity of the solutions of the riemann problem, *Transp. Res. Part B* 41 (7) (2007) 710–721.
- [25] S. Moutari, M. Rascle, A hybrid lagrangian model based on the aw-rasclé traffic flow model, *SIAM Journal on Applied Mathematics* 68 (2) (2007) 413–436.

- [26] S. Mammar, J.-P. Lebacque, H. H. Salem, Riemann problem resolution and godunov scheme for the aw-rascle-zhang model, *Transportation Science* 43 (4) (2009) 531–545.
- [27] S. Fan, M. Herty, B. Seibold, Comparative model accuracy of a data-fitted generalized aw–rascle–zhang model, *Networks and Heterogeneous Media* 9 (2) (2014) 239–268.
- [28] J. M. Greenberg, Congestion redux, *SIAM J. Appl. Math* 64 (2004) 1175–1185.
- [29] D. Chen, J. Laval, Z. Zheng, S. Ahn, A behavioral car-following model that captures traffic oscillations, *Transp. Res. Part B* 46 (6) (2012) 744–761.
- [30] M. Mauch, M. J. Cassidy, Freeway traffic oscillations: Observations and predictions, in: 15th Int. Symp. on Transportation and Traffic Theory, Elsevier, 2002, pp. 653–674.
- [31] B. Coifman, S. Krishnamurthy, X. Wang, Lane-change maneuvers consuming freeway capacity, in: *Traffic and Granular Flow 03*, Springer Berlin Heidelberg, 2005, pp. 3–14.
URL http://dx.doi.org/10.1007/3-540-28091-X_1
- [32] S. Ahn, C. M. J., Freeway traffic oscillations and vehicle lane-change maneuvers, in: 17Th Int. Symp. on Transportation and Traffic Theory, Elsevier, 2007, pp. 691–710.
- [33] Z. Zheng, S. Ahn, D. Chen, J. Laval, Freeway traffic oscillations: Microscopic analysis of formations and propagations using wavelet transform, *Trans. Res. Part B* 45 (9) (2011) 1378–1388.
- [34] X. Litrico, V. Fromion, *Modeling and control of hydrosystems*, Springer, 2009.
- [35] X. Litrico, V. Fromion, H-infinity control of an irrigation canal pool with a mixed control politics, *IEEE Transactions on Control Systems Technology* 14 (1) (2006) 99–111.
- [36] T. W. Sturm, *Open channel hydraulics*, McGraw-Hill, 2001.
- [37] A. Hofleitner, C. Claudel, A. Bayen, Reconstruction of boundary conditions from internal conditions using viability theory, in: *American Control Conference*, IEEE, 2012, pp. 640–645.